PAPER

Dodecahedral hollow multi-shelled Co₃O₄/Ag:ZnIn₂S₄ photocatalyst for enhancing solar energy utilization efficiency

Zhiman Liang,[a] Bobo Bai,[a] Xiufang Wang,[a] Yu Gao,*[a] Yi Li,[a] Qiuhui Bu,[a] Fu Ding, [ID] *[b] Yaguang Sun [ID] [b] and Zhenhe Xu [ID] *[a]

Employing semiconductor photocatalysts featuring a hollow multi-shelled (HoMs) structure to establish a heterojunction is an effective approach to addressing the issues of low light energy utilization and severe recombination of photogenerated charge carriers. To take advantage of these key factors in semiconductor photocatalysis, here, a dodecahedral HoMs Co_3O_4/Ag:ZnIn₂S₄ photocatalyst (denoted as Co_3O_4/AZIS) was firstly synthesized by coupling Ag^+-doped ZnIn₂S₄ (AZIS) nanosheets with dodecahedral HoMs Co_3O_4. The unique HoMs structure of the photocatalyst can not only effectively promote the separation and transfer of photo-induced charge, but also improve the utilization rate of visible light, exposing rich active sites for the photocatalytic redox reaction. The photocatalytic experiment results showed that the Co_3O_4/90.0 wt% AZIS photocatalyst has a high hydrogen (H_2) production rate (695.0 μmol h^{-1} g^{-1}) and high methyl orange (MO) degradation rate (0.4243 min^{-1}). This work provides a feasible strategy for the development of HoMs heterojunction photocatalysts with enhanced H_2 production and degradation properties of organic dyes.

1. Introduction

Energy constraints and environmental issues are obstacles to the sustainable development of human civilization, and the development of new green technologies for energy production is crucial for the whole of society.[1] Photocatalytic technology, a method of using solar energy to split water into clean hydrogen fuel, is widely seen as a promising solution to energy and environmental challenges.[2,3] However, the lack of efficient photocatalytic materials hinders the further application of this technology. In general, most single-component semiconductor photocatalytic materials have inherent defects, such as limited utilization of light energy, rapid recombination of photogenerated electrons (e^-) and holes (h^+), and restricted redox potential.[4,5] These issues are critical problems that result in poor photocatalytic activity. Therefore, various strategies have been proposed to further improve the photocatalytic performance, including defect engineering,[6] heterojunction engineering,[7,8] element doping,[9] and morphology control.[10–12] Among them, the morphology control strategy is an important method to improve the photocatalytic performance by adjusting the shape and structure of photocatalytic materials. Extensive

research has consistently demonstrated that photocatalysts with diverse morphologies manifest superior photocatalytic activity compared to bulk nanomaterials, as substantiated by numerous studies.[13] For example, one-dimensional photocatalysts such as nanowires and nanorods extend the diffusion path of photogenerated carriers through their high aspect ratio.[14,15] Two-dimensional materials such as nanosheets provide a larger specific surface area and more active sites with their lamellar structure.[16] Compared with one-dimensional and two-dimensional materials, three-dimensional materials (such as nanoflowers, porous/hollow structures, or core–shell structures) can achieve multiple reflections of incident light through an open frame, further improving light energy utilization efficiency.[17,18] Therefore, more and more researchers have begun to explore the use of three-dimensional materials as photocatalysts.

In recent years, HoMs, a novel three-dimensional structure composed of multiple sequentially arranged shell layers and cavities, has demonstrated enormous potential in various fields such as catalysis, waste treatment, and sensors.[19] Compared to traditional hollow and nanostructured materials, HoMs materials have a larger specific surface area, higher light energy utilization efficiency, and better loading capacity.[20] In the past 10 years, especially since the sequential templating approach was reported, more and more researchers have devoted themselves to the controlled synthesis of HoMs structure materials and its related applications. In 2009, Wang *et al.* successfully synthesized dodecahedral HoMs Co_3O_4 using the sequential

[a]College of Environmental and Chemical Engineering, Dalian University, Dalian 116622, China. E-mail: gaoy777@126.com; xuzh@syuct.edu.cn

[b]Key Laboratory of Inorganic Molecule-Based Chemistry of Liaoning Province, Shenyang University of Chemical Technology, Shenyang, 110142, China. E-mail: dingfu@syuct.edu.cn

templating approach by utilizing metal–organic frameworks as templates.[21] This photocatalyst inherits ordered structural information from the cobalt-based metal–organic framework material and exposes more active crystal facets (111) on its shell surface. As a result, it exhibits higher photocatalytic activity in the photoreduction of CO_2 reaction compared to ordinary HoMs structured materials. In addition, cobalt-based catalysts have garnered significant attention from researchers due to their cost-effectiveness, abundant content, thermodynamic stability, and environmental friendliness.[22] Unfortunately, achieving photocatalytic H_2 production on Co_3O_4 remains a challenge.[23] Researchers have proposed various strategies to address this issue. Among them, the preparation of heterojunction photocatalysts by coupling different semiconductor materials is considered to be one of the most effective approaches.[24] For example, Pan *et al.* prepared a $Co_3O_4/Ti^{3+}–TiO_2/NiO$ hollow core–shell dual pn junction through a continuous chemical-hydrothermal-annealing-reduction method, and the resulting $Co_3O_4/Ti^{3+}–TiO_2/NiO$ exhibited excellent photocatalytic H_2 production and selective photoreduction of CO_2.[25] Deng *et al.* utilized a facile microwave-assisted method to anchor $CsPbBr_3$ quantum dots onto the surface of Co_3O_4 nanocages derived from ZIF-67, and successfully constructed a p–n heterojunction photocatalyst with excellent photocatalytic CO_2 reduction performance.[26] The aforementioned cutting-edge researches suggest that constructing heterojunctions by combining materials with diverse energy level structures is an efficient approach to effectively address the issue of inadequate photocatalytic H_2 production performance in Co_3O_4.

$ZnIn_2S_4$ (ZIS) is a sulfide-based material with tunable direct band gap energy and excellent visible light absorption properties, showing great potential in the field of materials science.[27,28] However, the charge separation and migration efficiency of ZIS is inadequate, resulting in less than ideal photocatalytic H_2 production activity.[29] In recent years, our group has found that doping silver ions into ultra-thin ZIS nanosheets with a two-dimensional structure can significantly improve their photocatalytic activity.[30] This is because silver ions can enter the nanosheets through substitutional doping and interstitial doping, forming stable acceptor and donor states with atoms or vacancies.[31] This can significantly increase the number of charge carriers and improve the efficiency of charge transfer, thereby effectively enhancing photocatalytic activity. More importantly, AZIS can be coupled with other semiconductors through a simple water bath method to form heterojunctions.[30] Considering the above advantages, the combination of dodecahedral HoMs Co_3O_4 and AZIS nanosheets to construct heterojunctions is an effective way to overcome the poor photocatalytic activity of Co_3O_4. To the best of our knowledge, there is currently no available literature reporting on the utilization of the dodecahedral HoMs Co_3O_4/AZIS photocatalyst applied as a photocatalyst.

In this study, we have successfully designed and fabricated a highly efficient dodecahedral HoMs Co_3O_4/AZIS photocatalyst, which exhibits remarkable enhancement in both H_2 production and MO degradation activity under the visible light irradiation. The photocatalyst exhibits excellent photocatalytic performance due to the effective promotion of separation and migration of photogenerated $e^-–h^+$ by the formation of a type-II heterojunction between Co_3O_4 and AZIS, thereby suppressing severe recombination of photogenerated charge carriers. In addition, the dodecahedral HoMs Co_3O_4 not only exposes more reactive sites and shortens diffusion distance but also allows for multiple reflections/scattering of incident light within the photocatalyst, enhancing the utilization efficiency of visible light. The results of photocatalytic experiments show that the dodecahedral HoMs Co_3O_4/AZIS photocatalyst exhibits higher photocatalytic performance under visible light conditions (with a H_2 production rate of 695.0 $\mu mol\ h^{-1}\ g^{-1}$ and a MO degradation rate of 0.1406 min^{-1}) compared to the single dodecahedral HoMs Co_3O_4. In addition, we have conducted a detailed study on the energy level structure of the dodecahedral HoMs Co_3O_4/AZIS photocatalyst and have explored in depth its possible mechanisms in photocatalytic H_2 production and MO degradation.

2. Experimental section

2.1. Chemicals

Cobaltous nitrate hexahydrate ($Co(NO_3)_2 \cdot 6H_2O$, ≥99.99%), 2-methylimidazole (≥98.0%), methanol (≥99.5%), thiourea (≥99.0%), silver nitrate ($AgNO_3$, ≥99.8%), zinc acetate dihydrate ($Zn(OAc)_2 \cdot 2H_2O$, ≥99.0%), indium nitrate ($In(NO)_3$, ≥99.9%), L-cysteine (L-cys, ≥99.0%), thioacetamide (TAA, ≥98.0%), dimethylformamide (DMF, ≥99.5%), methyl orange (MO, ≥85.0%), triethanolamine (TEOA, ≥99.0%), 1,4-benzoquinone (BQ, ≥99.0%) (1 mM), disodium ethylenediaminetetraacetate (Na_2-EDTA, ≥99.0%) (1 mM), and *tert*-butyl alcohol (*t*-BuOH, ≥99.0%) (1 mM) were purchased from Aladdin Reagent Co. Ltd.

2.2. Synthesis of the dodecahedral ZIF-67

The dodecahedral zeolitic imidazolate framework-67 (ZIF-67) was synthesized using a typical synthetic method reported in the literature.[32] Two solutions were prepared by dissolving 7.50 mmol of $Co(NO_3)_2 \cdot 6H_2O$ and 32.30 mmol of 2-methylimidazole separately in solutions containing 30 mL methanol each. Then, the solution of 2-methylimidazole was quickly poured into the solution of $Co(NO_3)_2 \cdot 6H_2O$ and vigorously stirred for 10 minutes. Finally, the resulting mixed solution was kept at room temperature for 24 hours. The product was washed several times with anhydrous ethanol and then dried at 50 °C for 12 hours to obtain purple dodecahedral ZIF-67.

2.3. Synthesis of dodecahedral HoMs Co_3O_4

The obtained dodecahedral ZIF-67 was placed in a tubular furnace and heated at a rate of 1 °C per minute to 400 °C. After being calcined for 3 hours, dodecahedral HoMs Co_3O_4 could be obtained.

2.4. Synthesis of the dodecahedral HoMs Co_3O_4/AZIS photocatalysts

The dodecahedral HoMs Co_3O_4/AZIS photocatalysts were prepared using a simple water bath method. Under magnetic stirring, a certain amount of dodecahedral HoMs Co_3O_4 was introduced into 30 mL of a precast aqueous solution composed of the calculated amounts of $Zn(OAc)_2 \cdot 2H_2O$, $In(NO_3)_3$, $AgNO_3$, and

L-cys. After 30 minutes of magnetic stirring, the calculated amount of TAA was added and stirring continued to form a homogeneous solution. The solution was transferred into a 100 mL flask and reacted in a water bath at 95 °C for 3 hours. After the reaction, the solution was naturally cooled to room temperature, centrifuged to collect the precipitation, and washed several times with deionized water. Finally, the resulting black products were dried in a 70 °C oven for 12 hours. Meanwhile, different mass ratio samples of dodecahedral HoMs Co_3O_4/AZIS photocatalysts were fabricated using the same method with varying contents of AZIS at 85.0 wt%, 90.0 wt%, and 95.0 wt%.

2.5. Characterization

The X-ray diffraction (XRD) patterns of the samples were collected on a Bruker D8 Advance X-ray diffractometer with Cu Kα radiation (λ = 0.154 nm). TEM and high-resolution TEM (HRTEM) images of the as-samples were obtained using a JEM 2010 EX instrument at an accelerating voltage of 200 kV, which is equipped with an energy-dispersive X-ray (EDX) spectrometer. The UV-vis diffused reflectance spectra (DRS) of the samples were recorded on a UV-vis spectrophotometer (UV2550, Shimadzu) equipped with an integrating sphere, using $BaSO_4$ as the reflectance standard. X-ray photoelectron spectroscopy (XPS) measurements were conducted on a Thermal ESCALAB 250Xi electron spectrometer with Al Kα radiation X-ray source as the exciting source to determine the chemical states and the valence states of the involved elements. The photoelectrochemical (PEC) measurements were conducted using an electrochemical workstation (CHI 660E, CH Instruments) in a standard three-electrode system. In this system, the prepared sample film served as the working electrode, an Ag/AgCl electrode (3 M KCl) was used as the reference electrode, and Pt wire as the counter electrode. The working electrode was prepared on fluorine-doped tin oxide (FTO) glass. Firstly, 5 mg of photocatalyst was dissolved in 1 mL of DMF through ultrasonication to obtain a colloidal dispersion. Then, it was uniformly coated onto the FTO conductive glass. After natural air drying, the uncoated portion was isolated using epoxy resin adhesive. The electrolyte employed in the aforementioned measurements was an aqueous solution of Na_2SO_4 with a concentration of 0.2 M.

2.6. Photocatalytic H_2 production

A photocatalytic H_2 production automatic online analysis system (Labsolar-6A, Beijing Perfect Light) was used to test the photocatalytic properties of the prepared samples. In a typical experiment, 50 mg photocatalysts were uniformly dissolved into 50 mL mixed aqueous solution prepared by 40 mL of water and 10 mL of TEOA. The solution was transferred to a 100 mL quartz reactor and stirred continuously. Subsequently, the photocatalyst solution was vertically irradiated from above the quartz reactor using a 300 W xenon lamp (Beijing Perfect Light Source Co., Ltd.) equipped with a UV filter (λ > 420 nm). The temperature of the reaction solution was maintained at room temperature by a water-cooling system. The amount of H_2 produced by the photocatalytic reaction was analyzed by an online gas chromatography (GC-8860, TCD detector) with high-purity nitrogen as carrier gas. To examine the stability of the as-prepared photocatalysts, the photocatalysts were subjected to 20 cycles of H_2 production experiments, with a total exposure time of 100 hours.

2.7. Photodegradation of MO and detection of active species

Typically, 20 mL of MO dye solution (10 mg L^{-1}) and 10 mg of the prepared photocatalysts were added into a 100 mL quartz reactor. With the circulating water maintaining the reaction solution temperature, the suspension was magnetically stirred in the dark for 1 hour to reach the adsorption–dissociation equilibrium between the photocatalyst and MO. Subsequently, a xenon lamp (300 W, Beijing Perfect Light Source Co., Ltd.) equipped with ultraviolet cut-off filter (λ > 420 nm) was used as the light source. Under magnetic agitation, 1.5 mL of reaction liquid was taken out at regular intervals and the sediment was removed by centrifugation. A UV-vis spectrometer (Shimadzu UV-3600i Plus) was used to quantify the MO content of supernatant. Meanwhile, the recovered samples were tested 20 times under the same conditions to verify the stability of the prepared dodecahedral HoMs Co_3O_4/AZIS photocatalysts. In addition, in order to detect the active species generated during the photocatalytic degradation of MO, photodegradation experiments were conducted using different scavengers under the same conditions. Specifically, BQ, Na_2EDTA, and t-BuOH were used to trap superoxide radical ($^{\cdot}O_2^{-}$), h^+, and hydroxyl radical ($^{\cdot}OH$), respectively.

3. Results and discussion

The dodecahedral HoMs Co_3O_4/AZIS photocatalysts were synthesized by three-step synthesis route, as shown in Scheme 1. The TEM image shows that the synthesized ZIF-67 has a dodecahedral structure with a relatively smooth surface and
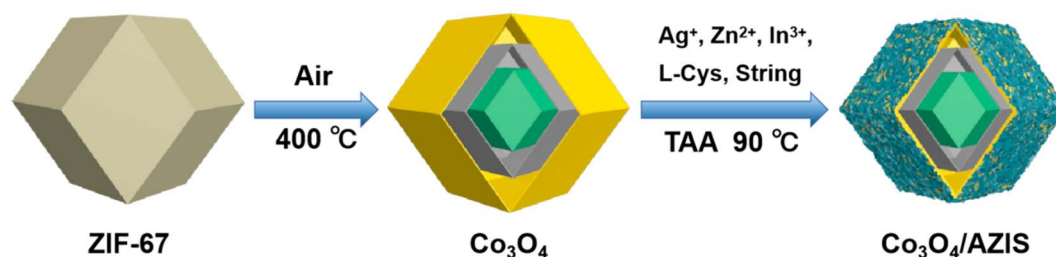
Scheme 1 Schematic illustration for the synthesis of dodecahedral HoMs Co_3O_4/AZIS photocatalyst.
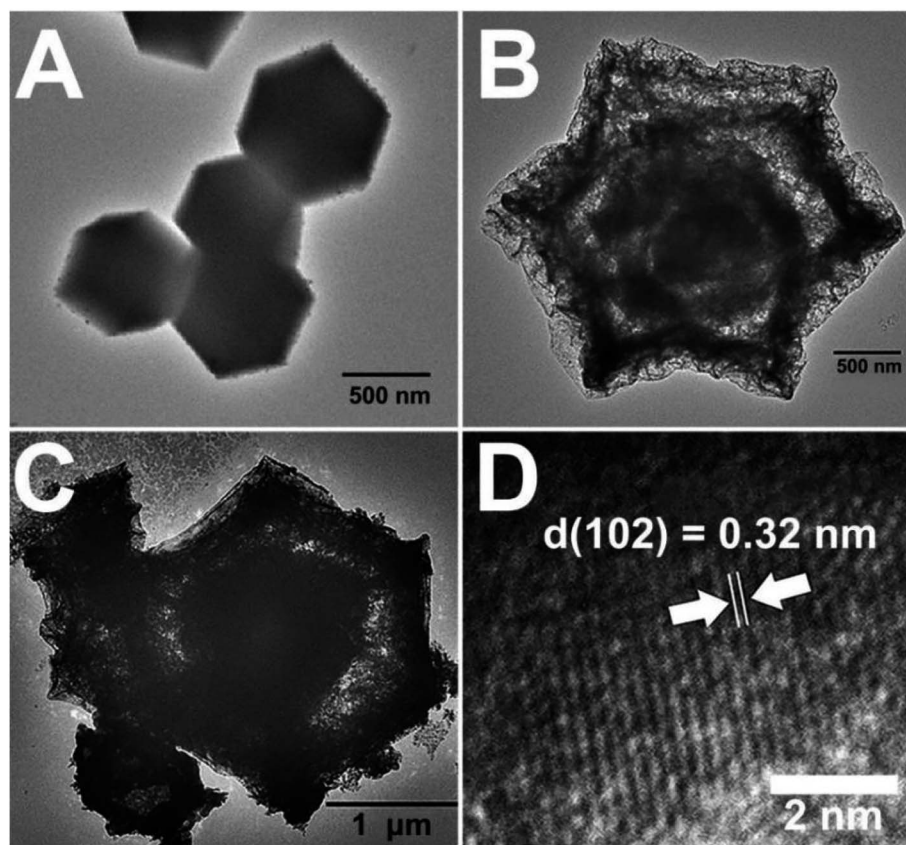
Fig. 1 TEM images of (A) ZIF-67, (B) Co_3O_4, and (C) Co_3O_4/90.0 wt% AZIS. (D) HRTEM image of the Co_3O_4/90.0 wt% AZIS.
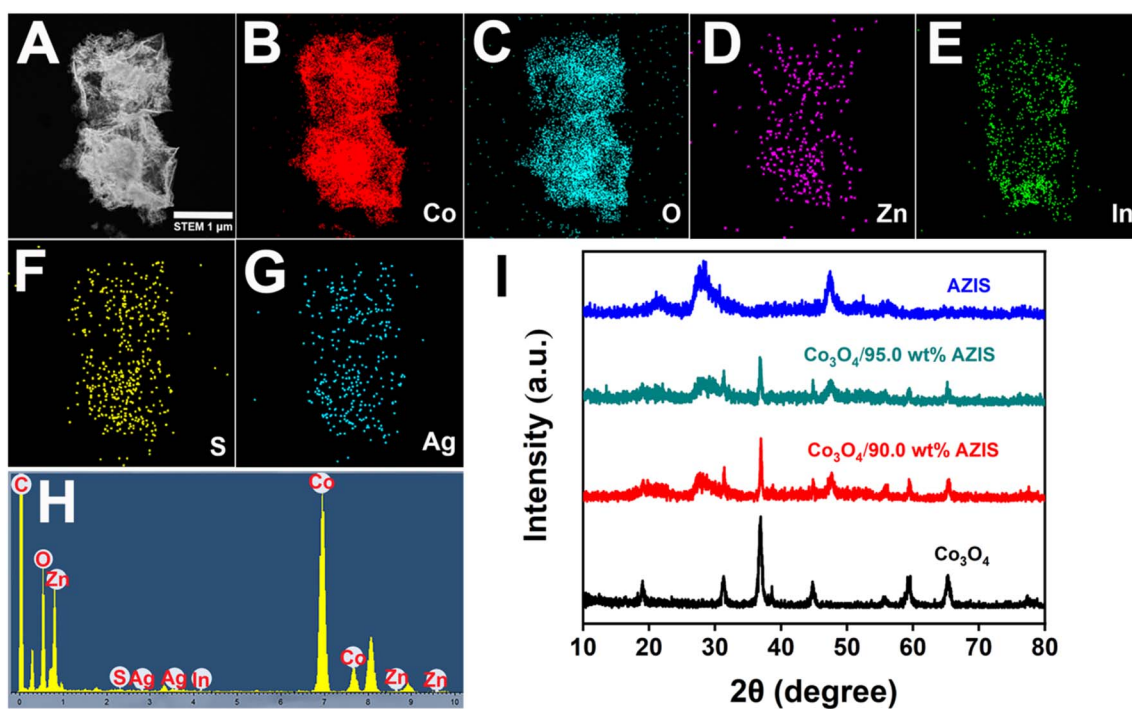

Fig. 2 (A) HAADF-STEM image of Co_3O_4/90.0 wt% AZIS, (B–G) the corresponding elemental mapping images of Co, O, Zn, In, S, and Ag elements, and (H) the corresponding EDX spectrum. (I) XRD patterns of Co_3O_4, AZIS, and Co_3O_4/AZIS.
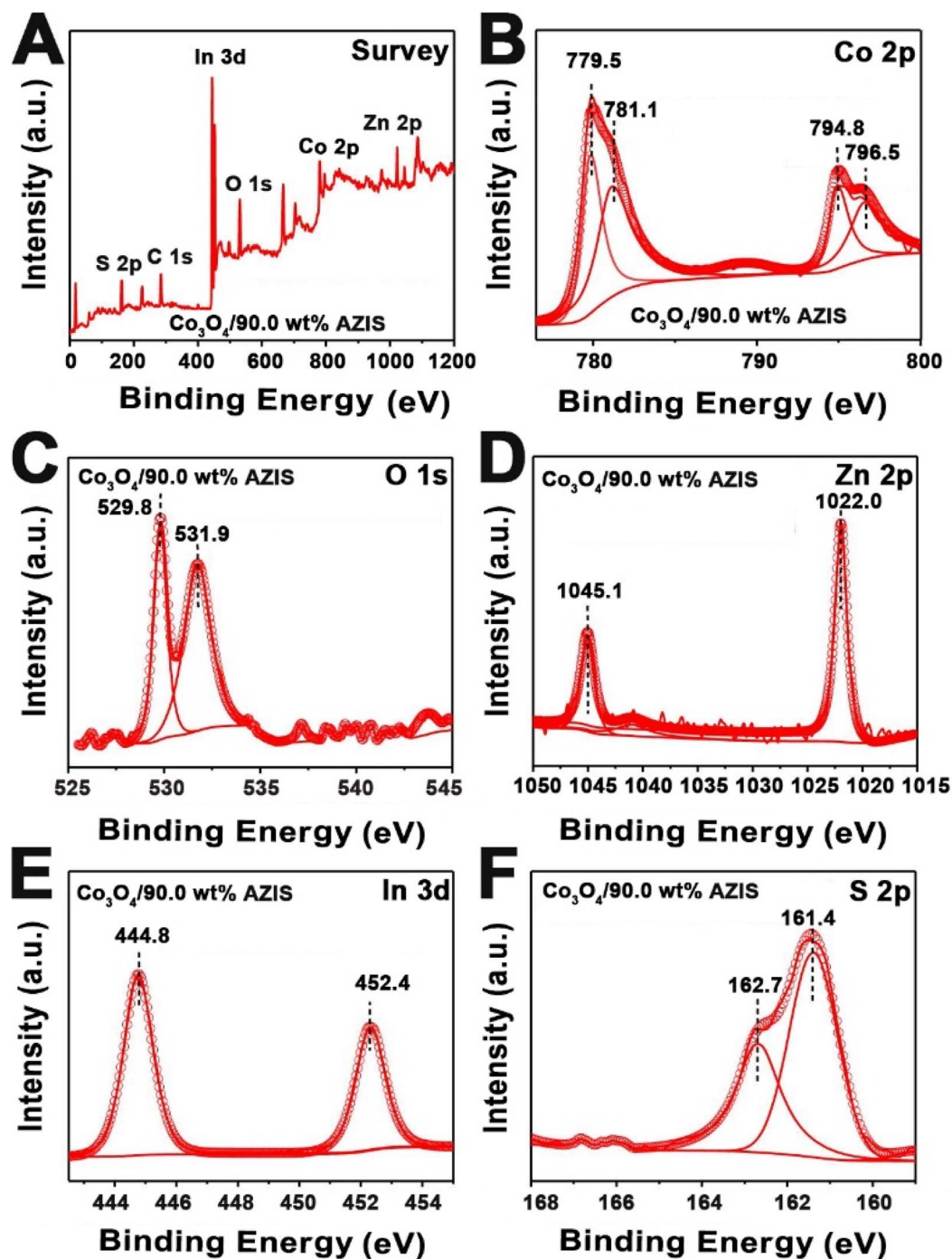
Fig. 3 XPS spectrum of Co₃O₄/90.0 wt% AZIS: (A) survey spectrum, and (B) Co 2p, (C) O 1s, (D) Zn 2p, (E) In 3d, and (F) S 2p high-resolution spectra.

an average size of 700 nm (Fig. 1A). As shown in Fig. 1B, the prepared Co_3O_4 inherits the dodecahedral structure of ZIF-67, with a size of approximately 2 μm. Interestingly, the morphology of the sample changes significantly after heat treatment due to partial collapse and fracture of the ZIF-67 framework, resulting in the formation of Co_3O_4 with a hollow triple-shell structure. Cavities with distances ranging from approximately 80 to 220 nm can be observed between the shells,

while the shell thickness ranges from 150 to 400 nm. In addition, unlike the smooth surface of dodecahedral ZIF-67, dodecahedral HoMs Co_3O_4 exhibits a honeycomb-like porous structure on its surface, which can expose more active sites and is beneficial for AZIS loading. Fig. 1C shows the TEM image of the dodecahedral HoMs Co_3O_4/AZIS photocatalyst, where a large number of AZIS nanosheets can be clearly observed randomly attached to the outer surface of the dodecahedral

HoMs Co_3O_4, indicating the formation of a heterostructure between Co_3O_4 and AZIS. In addition, it can be observed that the structure of the dodecahedral HoMs Co_3O_4/AZIS remains stable without significant collapse after the formation of heterojunctions through a water bath reaction, indicating its high stability. The HRTEM image (Fig. 1D) of the Co_3O_4/90.0 wt% AZIS reveals distinct lattice fringes with lattice spacing of 0.32 nm, consistent with the lattice spacing of the ZIS (102) plane.[31] In addition, by combining high-angle annular dark-field scanning transmission electron microscopy (HAADF-STEM) images (Fig. 2A), along with corresponding elemental mapping images (Fig. 2B–G) and EDX spectrum (Fig. 2H), we are able to confirm the composition of the Co_3O_4/AZIS. The results show that the composite photocatalyst is composed of elements Co, O, Zn, In, S, and Ag, and these elements are uniformly distributed in the dodecahedral HoMs Co_3O_4/AZIS photocatalyst.

Fig. 2I shows the XRD patterns of the as-prepared samples. For pure Co_3O_4, the characteristic peaks appeared at 19.0°, 31.3°, 36.9°, 38.7°, 44.8°, 55.8°, 59.4° and 65.3° correspond to the crystal planes (111), (220), (311), (222), (400), (422), (511) and (440) of Co_3O_4 (JCPDS card no. 42-1467), respectively.[21] For the AZIS, it can be seen that all the peaks of the sample can be well indexed to the hexagonal phase ZIS according to the JCPDS card no. 72-0773.[33] The absence of any unrecognizable diffraction peaks indicates that Ag^+ ions are successfully incorporated into the lattice of ZIS without forming a separate phase. As expected, the dodecahedral HoMs Co_3O_4/AZIS photocatalyst prepared in this study has the characteristic peaks of both Co_3O_4 and ZIS. Interestingly, as the AZIS content increases, the characteristic peak intensity of Co_3O_4 decreases, indicating the successful formation of a heterojunction between Co_3O_4 and AZIS.

An XPS test was performed to further determine the elemental composition and chemical valence state of the Co_3O_4/90.0 wt% AZIS. From the full XPS spectrum (Fig. 3A), we can not only detect Co and O elements from Co_3O_4, but also Zn, In, and S elements from AZIS, further confirming the successful coupling of Co_3O_4 with AZIS. As presented in Fig. 3B, the high-resolution Co 2p spectrum is split into two sets of spin–orbit double peaks. Among them, the peaks at 779.5, 794.8, 781.1, and 796.5 eV are attributed to Co^{3+} $2p_{3/2}$, Co^{3+} $2p_{1/2}$, Co^{2+} $2p_{3/2}$, and Co^{2+} $2p_{1/2}$, respectively, indicating the presence of Co^{2+} and Co^{3+}.[34] In the high-resolution O 1s spectrum (Fig. 3C), the peaks at 529.8 eV and 531.9 eV are assigned to metal–oxygen bond and chemisorbed oxygen species, respectively.[35] As shown in Fig. 3D, two typical peaks at 1022.0 and 1045.1 eV correspond to Zn $2p_{3/2}$ and $2p_{1/2}$ of Zn^{2+} in the AZIS, respectively. The high-resolution In 3d spectrum (Fig. 3E) exhibits two distinct peaks at binding energies of approximately 452.4 and 444.8 eV, which are assigned to In $3d_{3/2}$ and In $3d_{5/2}$, respectively.[36] For S 2p spectrum (Fig. 3F), two splitting peaks originating from S $2p_{3/2}$ and $2p_{1/2}$ are located at near 161.4 and 162.7 eV, respectively, indicating that S in Co_3O_4/AZIS exists in the state of S^{2-}.[36]

The light absorption capacity of photocatalysts is one of the pivotal factors that affect its photocatalytic performance. To investigate the solar light harvesting capacity of the prepared samples, an analysis of UV-vis DRS was conducted. Fig. 4A

clearly demonstrates that pure Co_3O_4 has a broad absorption wavelength range, enabling it to absorb both UV and visible light, which is consistent with previous research.[37] For AZIS, the absorption edge appears at around 500 nm. After the formation of a heterojunction between Co_3O_4 and AZIS, the visible light absorption intensity is significantly enhanced compared to single-phase AZIS. As the proportion of Co_3O_4 increases, the absorption edge of the composite material gradually redshifts, which corresponds to the color change of the sample.
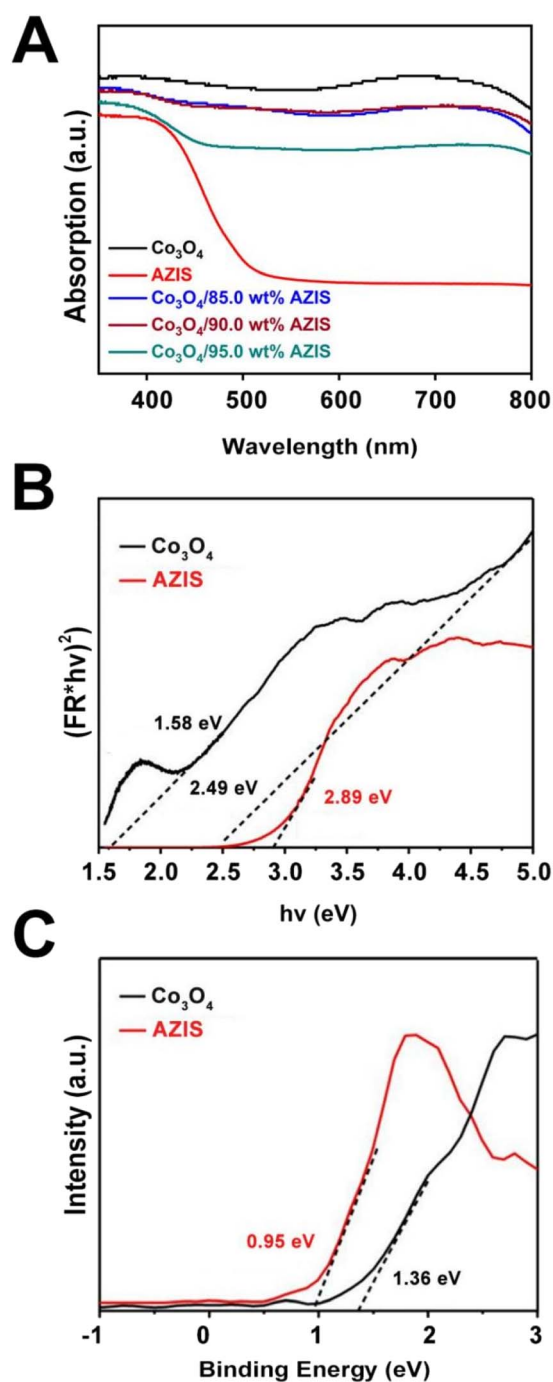

Fig. 4 (A) UV-vis DRS spectra of Co_3O_4, AZIS, and Co_3O_4/AZIS. (B) The band gap energy and (C) UPS spectra of the Co_3O_4 and AZIS.
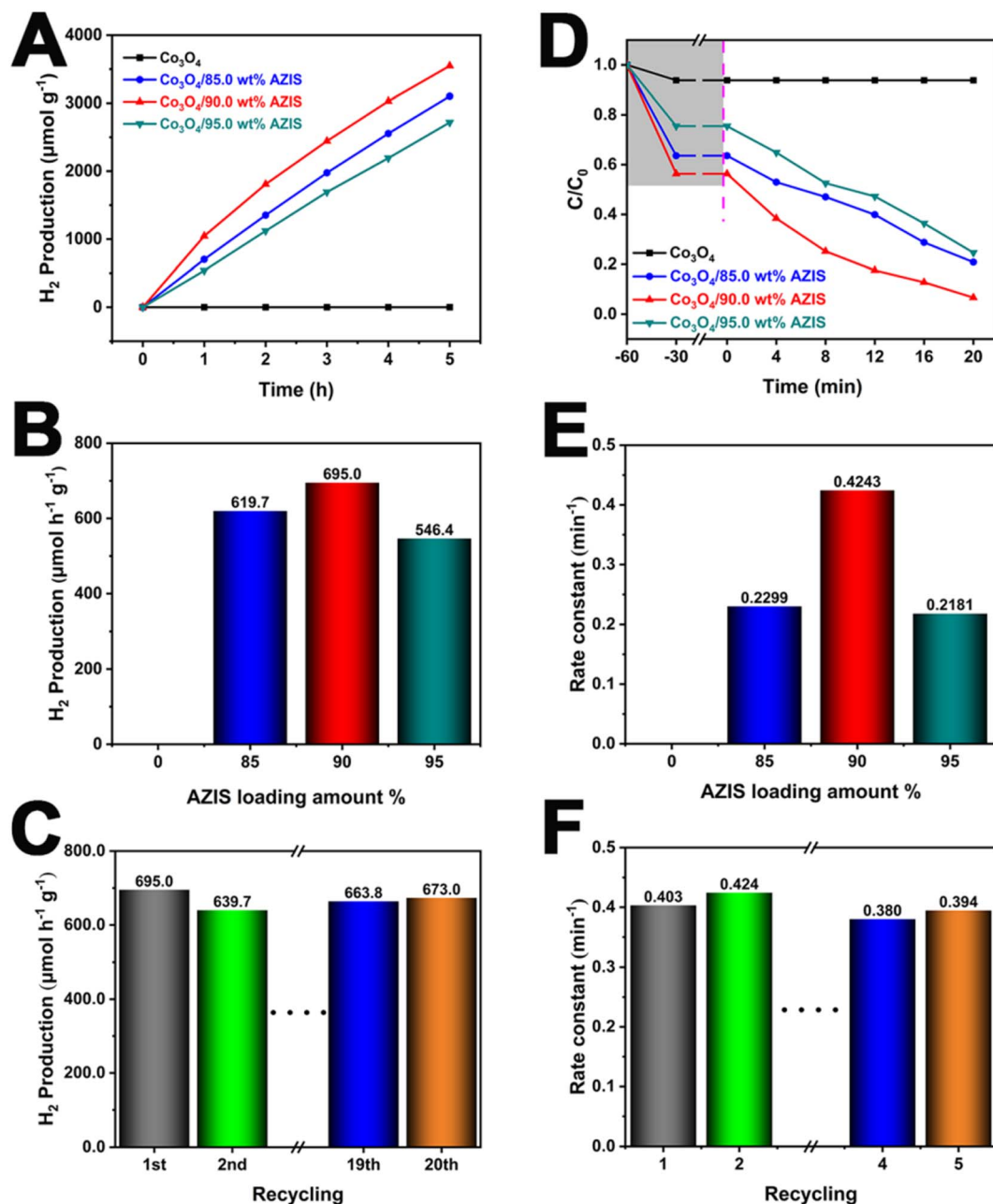
Fig. 5 (A) The photocatalytic H_2 production of Co_3O_4 and Co_3O_4/AZIS under visible light irradiation, and (B) the corresponding photocatalytic H_2 production rates. (C) Stability study of Co_3O_4/90.0 wt% AZIS for the photocatalytic H_2 production. (D) The photocatalytic MO degradation curve of Co_3O_4 and Co_3O_4/AZIS, and (E) the corresponding photocatalytic degradation rate of MO. (F) Stability study of Co_3O_4/90.0 wt% AZIS for the MO photocatalytic degradation.

Therefore, the heterojunctions constructed between Co_3O_4 and AZIS can fully enhance the light absorption range and intensity. Furthermore, the band gaps (E_g) of Co_3O_4 and AZIS are calculated using the formula:

$$\alpha h\nu = A(h\nu - E_g)^{n/2}$$

in which α is the absorption coefficient, A is a constant, $h\nu$ is the photon energy (eV), n is dependent on the type of semiconductor (for Co_3O_4 and AZIS, $n = 4$),[38,39] and E_g is the bandgap

value. As depicted in Fig. 4B, the E_g of Co_3O_4 and AZIS can be obtained by linear partial extrapolation to about 2.49 and 2.89 eV respectively. At the same time, according to the ultraviolet photoelectron spectrum (UPS), we can obtain the energy values corresponding to the valence band (VB) positions of Co_3O_4 and AZIS as 1.36 eV and 0.95 eV, respectively (Fig. 4C). Furthermore, we can calculate the conduction band (CB) potentials of Co_3O_4 and AZIS using the following formula:
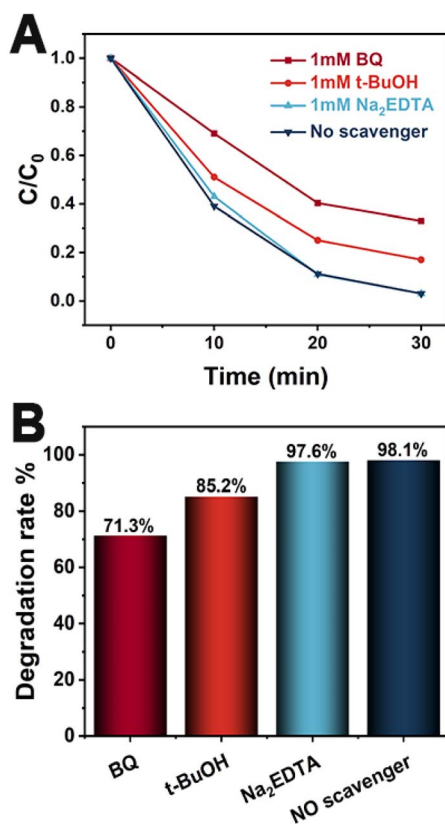
$$E_{CB} = E_{VB} - E_g$$

Fig. 6 (A) Variation trend in MO concentration over time in the presence of Co_3O_4/90.0 wt% AZIS and three different scavengers (B) the corresponding summaries of degradation percentage after 30 min irradiation.

Therefore, the CB potentials of Co_3O_4 and AZIS are about −1.13 and −1.94 eV, respectively.

Photocatalytic H_2 production experiments were conducted under visible light irradiation to evaluate and compare the activities of the prepared samples. Fig. 5A shows the trend of the photocatalytic H_2 production of the prepared samples with the reaction time. It can be seen from the figure that with the increase of reaction time, the H_2 production of all the composite photocatalysts increases approximately in a straight line, indicating that the performance of the synthesized composite photocatalysts is stable. In addition, it can be seen that the H_2 production of pure Co_3O_4 is zero as the reaction time increases. Fig. 5B shows the order of H_2 production rates for all samples: Co_3O_4/90.0 wt% AZIS (695.0 μmol h^{-1} g^{-1}) > Co_3O_4/85.0 wt% AZIS (619.7 μmol h^{-1} g^{-1}) > Co_3O_4/95.0 wt% AZIS (546.4 μmol h^{-1} g^{-1}) > Co_3O_4 (0 μmol h^{-1} g^{-1}). Specifically, when the AZIS loading increases from 85.0 wt% to 90.0 wt%, the photocatalytic H_2 production rate continued to increase, reaching a maximum value of 695.0 μmol h^{-1} g^{-1} at 90.0 wt%. However, as the loading of AZIS continues to increase, the photocatalytic H_2 production rate decreases, which is caused by the shielding effect of excessive AZIS on the reaction site. In addition, in order to evaluate the stability of Co_3O_4/AZIS, we conducted a 20-cycle (100 hours) photocatalytic H_2 production

experiment under visible light irradiation. As shown in Fig. 5C, no significant decay is observed in 20 cycles, demonstrating the high stability of the dodecahedral HoMs Co_3O_4/90.0 wt% AZIS photocatalyst in the photocatalytic H_2 production.

In order to further determine the photocatalytic degradation MO performance of dodecahedral HoMs Co_3O_4/AZIS photocatalyst, photocatalytic degradation experiments were carried out. Fig. 5D illustrates the trend of MO concentration variation with reaction time for different ratios of photocatalysts. Compared to the Co_3O_4 without photocatalytic activity, all composite materials exhibit significantly higher photocatalytic activity. Particularly, Co_3O_4/90.0 wt% AZIS achieves a degradation rate of 96.8% in just 20 minutes of visible light irradiation. As shown in Fig. 5E, the MO removal rate constants of the samples followed the order of Co_3O_4/90.0 wt% AZIS (0.4243 min^{-1}) > Co_3O_4/85.0 wt% AZIS (0.2299 min^{-1}) > Co_3O_4/95.0 wt% AZIS (0.2181 min^{-1}) > Co_3O_4 (0 min^{-1}). The apparent effect of AZIS loading on photodegradation activity is consistent with the effect of photocatalytic H_2 production. Similarly, the photodegradation activity increases with the increase of AZIS loading. When it reaches 90.0 wt%, the photodegradation rate reaches its maximum (0.4243 min^{-1}). As the loading continues to increase, the photocatalytic activity decreases. Furthermore, in order to evaluate the stability of Co_3O_4/90.0 wt% AZIS as a photocatalyst for MO photodegradation, we performed 20 cycle tests. In Fig. 5F, it can be observed that the photocatalytic activity remains essentially unchanged for Co_3O_4/90.0 wt% AZIS, demonstrating good stability and reliability.

The radical trapping experiment was conducted to detect the main active species in the photocatalytic process. Fig. 6A shows the variation trend of MO concentration over time in the presence of Co_3O_4/90.0 wt% AZIS with three different scavengers. The variation trend of MO concentration in the system with added Na_2EDTA is consistent with the variation trend in the system without added scavengers, indicating that the presence of Na_2EDTA does not affect the degradation activity of MO. However, when BQ is added, the photocatalytic activity significantly decreases. In addition, when t-BuOH is added, the photocatalytic activity also slightly decreases. Fig. 6B shows the degree of decrease in photodegradation rate after adding various scavengers. Specifically, the addition of BQ significantly reduces the photocatalytic rate and leads to a decrease in degradation rate of 26.8%. Next is t-BuOH, which results in a decrease in degradation rate of 12.9%. However, with the addition of Na_2EDTA, there is no significant change in photocatalytic activity. This indicates that $^{\cdot}O_2^-$ plays a major role in the photocatalytic degradation of MO, while $^{\cdot}OH$ has a lesser effect and h^+ has almost no influence.

In order to determine the separation and recombination efficiency of photogenerated charges in Co_3O_4/AZIS, photoelectrochemical characterization was carried out. The transient photocurrent density curves of the Co_3O_4/90.0 wt% AZIS and Co_3O_4 are shown in Fig. 7A. In a total of 10 on/off cycles, the photocurrent density of the photocatalyst increases sharply when the light source is on and decreases sharply after the light source is off, indicating that the increased current is generated due to the introduction of light. The photocurrent density of
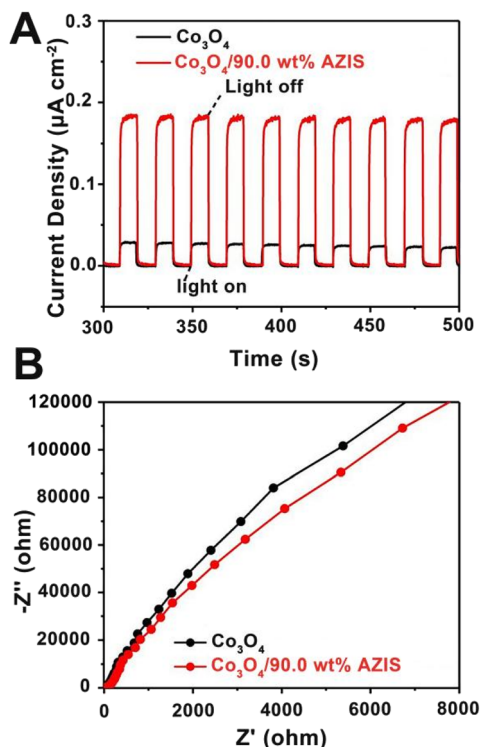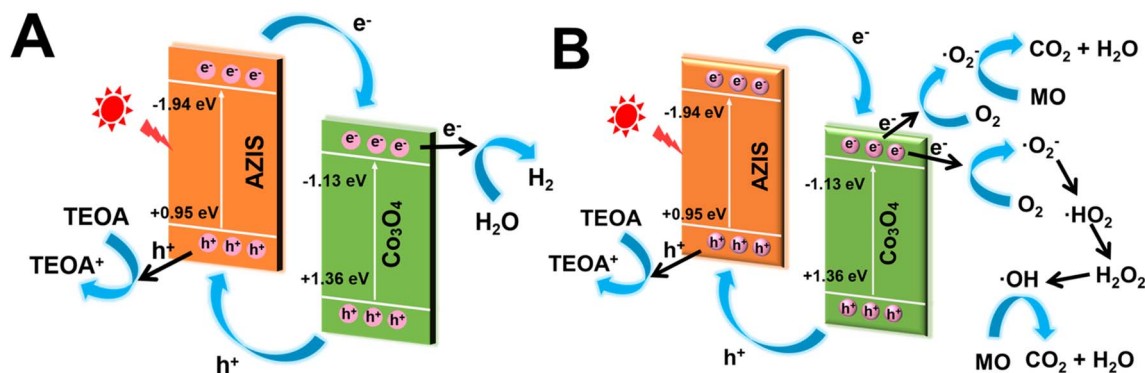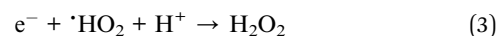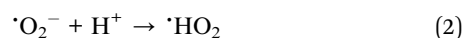
Fig. 7 (A) The transient photocurrent density curves and (B) the EIS Nyquist plots of Co_3O_4 and Co_3O_4/90.0 wt% AZIS.

Co_3O_4/90.0 wt% AZIS (0.18 μA cm^{-2}) is about 6 times than that of Co_3O_4 (0.03 μA cm^{-2}), which indicates that the heterojunction between Co_3O_4 and AZIS can effectively promote the photogenerated carrier separation and rapid migration. This argument is further supported by electrochemical impedance spectroscopy (EIS) testing (Fig. 7B), where Co_3O_4/90.0 wt% AZIS exhibits a smaller semicircle diameter compared to Co_3O_4, indicating reduced charge transfer resistance that facilitates charge transfer and inhibits charge recombination. The above results indicate that the construction of a dodecahedral HoMs Co_3O_4/AZIS photocatalyst is conducive to promoting the separation/migration of photogenerated e$^-$ and h$^+$, thus improving the photocatalytic activity.

Based on the aforementioned analysis and discussion, the photocatalytic mechanism and charge carrier transfer path of the dodecahedral HoMs Co_3O_4/AZIS photocatalyst were shown in Scheme 2. Under visible light irradiation, both Co_3O_4 and AZIS are excited to produce e$^-$ and h$^+$. As calculated above, the CB potential of AZIS (-1.94 eV) is more negative than that of Co_3O_4 (-1.13 eV), and the VB potential of Co_3O_4 (1.36 eV) is more positive than that of AZIS (0.95 eV); thus, the combination of Co_3O_4 and AZIS can form a type-II heterojunction. Driven by the potential difference, the photogenerated e$^-$ can quickly migrate from the CB of AZIS to the CB of Co_3O_4, and the photogenerated h$^+$ can quickly migrate from the VB of Co_3O_4 to the VB of AZIS. Therefore, the photogenerated e$^-$–h$^+$ pairs on the Co_3O_4/AZIS heterojunction can be effectively separated. In the case of photocatalytic H$_2$ production (Scheme 2A), the strongly reducing e$^-$ accumulated on the CB of Co_3O_4 can reduce H$_2$O to H$_2$, and the h$^+$ accumulated on the VB of AZIS is captured by TEOA. In the case of photocatalytic MO degradation (Scheme 2B), the strong reducing e$^-$ accumulated on the CB of Co_3O_4 combines with dissolved O$_2$ in water to form $\cdot O_2^-$ (O$_2$/$\cdot O_2^-$ = -0.33 eV) (eqn (1)); the $\cdot O_2^-$ has a strong oxidizing ability and can react with MO on the surface of the photocatalyst to achieve degradation (eqn (5)).[40,41] In addition, $\cdot$OH can produce by the e$^-$ on the CB of Co_3O_4 through a two-electron oxidation process.[42,43] Specifically, the $\cdot O_2^-$ generated by eqn (1) can also react with H$^+$ to form the peroxy hydroxyl radical ($\cdot$HO$_2$) (eqn (2)).[44,45] Then, the $\cdot$HO$_2$ further reacts with the e$^-$ on the CB of Co_3O_4 and H$^+$ to produce hydrogen peroxide (H$_2$O$_2$) (eqn (3)). Finally, the H$_2$O$_2$ undergoes a reaction with the e$^-$ on the CB of Co_3O_4 to generate $\cdot$OH (eqn (4)).[46,47] Therefore, the formed $\cdot$OH can also participate in the degradation of MO (eqn (6)). The main reactions involved in the process of MO photodegradation are as follows:

$$e^- + O_2 \rightarrow \cdot O_2^- \tag{1}$$

$$\cdot O_2^- + H^+ \rightarrow \cdot HO_2 \tag{2}$$

$$e^- + \cdot HO_2 + H^+ \rightarrow H_2O_2 \tag{3}$$

$$H_2O_2 + e^- \rightarrow \cdot OH + OH^- \tag{4}$$

Scheme 2 Schematic illustration of the possible mechanisms for (A) the photocatalytic H$_2$ production and (B) the MO degradation on the dodecahedral HoMs Co_3O_4/AZIS photocatalyst under visible light irradiation.

$$\cdot O_2{}^- + MO \rightarrow H_2O + CO_2 \qquad (5)$$

$$\cdot OH + MO \rightarrow H_2O + CO_2 \qquad (6)$$
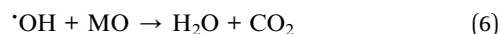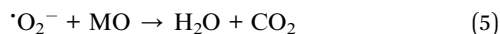
4. Conclusion

In summary, a novel dodecahedral HoMs Co_3O_4/AZIS photocatalyst was prepared by a simple water bath method and applied to photocatalytic H_2 production and MO degradation. The mechanism analysis shows that the type-II heterostructures formed between Co_3O_4 and AZIS can effectively promote the photogenerated carrier separation and improve the photocatalytic performance. Compared to dodecahedral HoMs Co_3O_4, the dodecahedral HoMs Co_3O_4/AZIS photocatalyst exhibits significantly enhanced photocatalytic activities. This study not only provides a simple strategy for *in situ* growth of AZIS nanosheets on dodecahedral Co_3O_4 HoMS surfaces, but also provides useful insights for the development of low-cost cobalt-based catalysts.

Conflicts of interest

The authors declare no competing interest.

Acknowledgements

References

1 A. Raja, N. Son, M. Swaminathan and M. Kang, *J. Clean. Prod.*, 2023, **423**, 138809.
2 A. Raja, N. Son, M. Swaminathan and M. Kang, *Chem. Eng. J.*, 2023, **468**, 143740.
3 S. Wang, Y. Wang, S. L. Zhang, S. Q. Zang and X. W. D. Lou, *Adv. Mater.*, 2019, **31**, 1903404.
4 Q. Zhang, J. Deng, Z. Xu, M. Chaker and D. Ma, *ACS Catal.*, 2017, **7**, 6225–6234.
5 M. Sun, R. T. Gao, J. He, X. Liu, T. Nakajima, X. Zhang and L. Wang, *Angew. Chem., Int. Ed.*, 2021, **60**, 17601–17607.
6 D. Maarisetty and S. S. Baral, *J. Mater. Chem. A*, 2020, **8**, 18560–18604.
7 Q. Zhang, S. Huang, J. Deng, D. T. Gangadharan, F. Yang, Z. Xu, G. Giorgi, M. Palummo, M. Chaker and D. Ma, *Adv. Funct. Mater.*, 2019, **29**, 1902486.
8 Q. Zhang, F. Yang, S. Zhou, N. Bao, Z. Xu, M. Chaker and D. Ma, *Appl. Catal., B*, 2020, **270**, 118879.
9 H. F. Li, K. W. Yu, X. B. Jing, L. Duan and Y. Y. Zhang, *Rare Met.*, 2024, DOI: 10.1007/s12598-023-02473-z.
10 W. Xu, W. Xie and Y. Wang, *ACS Appl. Mater. Interfaces*, 2017, **9**, 28642–28649.
11 A. Savateev, I. Ghosh, B. König and M. Antonietti, *Angew. Chem., Int. Ed.*, 2018, **57**, 15936–15947.
12 D. Zheng, X. N. Cao and X. Wang, *Angew. Chem., Int. Ed.*, 2016, **55**, 11512–11516.
13 R. t. Guo, J. Wang, Z. x. Bi, X. Chen, X. Hu and W. g. Pan, *Small*, 2022, **19**, 2206314.
14 A. Raja, N. Son and M. Kang, *J. Taiwan Inst. Chem. Eng.*, 2023, **144**, 104762.
15 N. Yu, R. Dong, J. Liu, K. Huang and B. Geng, *RSC Adv.*, 2016, **6**, 103938–103943.
16 Y. Jiang, H. Y. Chen, J. Y. Li, J. F. Liao, H. H. Zhang, X. D. Wang and D. B. Kuang, *Adv. Funct. Mater.*, 2020, **30**, 2004293.
17 Y. Wang, Z. Zhang, L. Zhang, Z. Luo, J. Shen, H. Lin, J. Long, J. C. S. Wu, X. Fu, X. Wang and C. Li, *J. Am. Chem. Soc.*, 2018, **140**, 14595–14598.
18 Y. Wei, N. Yang, K. Huang, J. Wan, F. You, R. Yu, S. Feng and D. Wang, *Adv. Mater.*, 2020, **32**, 8442–8449.
19 J. Zhao, J. Wang, R. Bi, M. Yang, J. Wan, H. Jiang, L. Gu and D. Wang, *Angew. Chem.*, 2021, **133**, 25923–25926.
20 N. Pan, M. Lin, H. Cui, W. Fan, C. Liu, F. Chen, C. Fan, Y. Xia and K. Sui, *Chem. Mater.*, 2020, **32**, 8442–8449.
21 L. Wang, J. Wan, Y. Zhao, N. Yang and D. Wang, *J. Am. Chem. Soc.*, 2019, **141**, 2238–2241.
22 L. Han, S. Dong and E. Wang, *Adv. Mater.*, 2016, **28**, 9266–9291.
23 X. Guo, X. Liu, M. Wang, J. Yan, Y. Chen and S. Liu, *Small*, 2023, **19**, 2206695.
24 H. Wang, L. Zhang, Z. Chen, J. Hu, S. Li, Z. Wang, J. Liu and X. Wang, *Chem. Soc. Rev.*, 2014, **43**, 5234.
25 J. Pan, G. Xiao, J. Niu, Y. Fu, J. Cao, J. Wang, Y. Zheng, M. Zhu and C. Li, *J. Clean. Prod.*, 2022, **380**, 135037.
26 X. Deng, Q. Liang, J. Fan, X. Yan, H. Si, H. Huang, Z. Li and Z. Kang, *Chem. Eng. J.*, 2023, **475**, 14638.
27 A. Raja, N. Son, S. Pandey and M. Kang, *Sep. Purif. Technol.*, 2022, **293**, 121119.
28 A. Raja, N. Son and M. Kang, *Appl. Surf. Sci.*, 2023, **607**, 155087.
29 H. Liu, J. Zhang and D. Ao, *Appl. Catal., B*, 2018, **221**, 433–442.
30 Y. Gao, B. Xu, M. Cherif, H. Yu, Q. Zhang, F. Vidal, X. Wang, F. Ding, Y. Sun, D. Ma, Y. Bi and Z. Xu, *Appl. Catal., B*, 2020, **279**, 119403.
31 Y. Gao, K. Qian, B. Xu, F. Ding, V. Dragutan, I. Dragutan, Y. Sun and Z. Xu, *RSC Adv.*, 2020, **10**, 32652–32661.
32 R. Banerjee, A. Phan, B. Wang, C. Knobler, H. Furukawa, M. O'Keeffe and O. M. Yaghi, *Science*, 2008, **319**, 939–943.
33 Y. Dou, Z. Liang, Z. Xu, Y. Wang, J. Zheng, D. Ma and Y. Gao, *ACS Appl. Nano Mater.*, 2023, **6**, 12537–12547.
34 W. Yan, Y. Xu, S. Hao, Z. He, L. Wang, Q. Wei, J. Xu and H. Tang, *Inorg. Chem.*, 2022, **61**, 4725–4734.
35 H. Yang, H. Sun, X. Fan, X. Wang, Q. Yang and X. Lai, *Mater. Chem. Front.*, 2021, **5**, 259–267.
36 Z. Zhang, L. Huang, J. Zhang, F. Wang, Y. Xie, X. Shang, Y. Gu, H. Zhao and X. Wang, *Appl. Catal., B*, 2018, **233**, 112–119.
37 H. Chen, C. Xue, D. Cui, M. Liu, Y. Chen, Y. Li and W. Zhang, *RSC Adv.*, 2020, **10**, 15245–15251.

38 M. Tang, Y. Ao, P. Wang and C. Wang, *J. Hazard. Mater.*, 2020, **387**, 121713.

39 Y. Wang, C. Zhu, G. Zuo, Y. Guo, W. Xiao, Y. Dai, J. Kong, X. Xu, Y. Zhou, A. Xie, C. Sun and Q. Xian, *Appl. Catal., B*, 2020, **278**, 119298.

40 X. Zhang, Y. Liu, X. Xiao and W. Zhou, *Chin. J. Org. Chem.*, 2022, **42**, 3890–3895.

41 W. Li, F. Wang, Y. Shi and L. Yu, *Chin. Chem. Lett.*, 2023, **34**, 107505.

42 Y. Cui, J. Huang, X. Fu and X. Wang, *Catal. Sci. Technol.*, 2012, **2**, 1396–1402.

43 L. Q. Ye, J. Y. Liu, Z. Jiang, T. Y. Peng and L. Zan, *Appl. Catal., B*, 2013, **142**, 1–7.

44 H. Zhou, X. Jing, P. Li and H. Cao, *Chin. J. Org. Chem.*, 2022, **42**, 1849–1855.

45 D. Yong, J. Tian, R. Yang, Q. Wu and X. Zhang, *Chin. J. Org. Chem.*, 2023, DOI: **10.6023/cjoc202310020**.

46 Y. Zhang, W. Li, Z. Hu, X. Jing and L. Yu, *Chin. Chem. Lett.*, 2024, **35**, 108938.

47 Y. Chen, C. Chen, Y. Liu and L. Yu, *Chin. Chem. Lett.*, 2023, **34**, 108489.